Simulations of crescent water wave patterns on finite depth

Ø. Kristiansen, D. Fructus, D. Clamond, and J. Grue
Department of Mathematics, University of Oslo, P.O. Box 1053 Blindern, NO-0316 Oslo, Norway

(Received 15 October 2004; accepted 14 March 2005; published online 16 May 2005)

A numerical study of the instabilities of Stokes waves on finite depth has been carried out using an efficient fully nonlinear method [D. Clamond and J. Grue, "A fast method for fully nonlinear water-wave computations," J. Fluid Mech. **447**, 337 (2001)]. First, attention is given to five-wave instabilities with $k_0h=O(1)$, k_0 being the wavenumber and h the depth. Both instabilities leading to breaking and instabilities leading to recurrence are studied, yielding considerably different patterns than on infinite depth. Higher-order instabilities are exemplified, for the first time, by simulations of six- and seven-wave instabilities. Simulations of interactions between four- and five-wave instabilities show that a classical modulational instability can destabilize a three-dimensional perturbation causing crescent waves to appear, in accordance with the hypothesis of [M.-Y. Su and A. W. Green, "Coupled two- and three-dimensional instabilities of surface gravity waves," Phys. Fluids **27**, 2595 (1984)]. Also, a recurrent five-wave instability can boost the energy in a four-wave instability. © *2005 American Institute of Physics*. [DOI: 10.1063/1.1920351]

I. INTRODUCTION

Crescent formed patterns are observed on longcrested waves moving along the surface of the ocean. Such patterns are studied experimentally in laboratories in the form of three-dimensional patterns developing on regular Stokes waves.[1–3] The experiments, which have been made on deep water with high Stokes wave steepnesses, typically show the growth of crescent or horseshoe patterns until breaking occurs. The observed patterns have a longitudinal periodicity that is a multiple of the length of the carrier wave, where a factor of two corresponds to the most frequently observed pattern (called L_2 pattern by Su[1]). Collard and Caulliez[4] reported a new pattern which they called an oscillating horseshoe pattern. The peaks oscillated back and forth transversally, but were longitudinally aligned (i.e., L_1 pattern). For all these experiments, it is accepted that the crescent formed patterns are triggered by the class II five-wave instability[5–7] of Stokes waves. This instability dominates over class I four-wave instabilities for high Stokes wave steepnesses.

Numerical simulations of crescent wave patterns were first made by Stiassnie and Shemer,[8] using the conservative Zakharov equation. Shrira, Badulin, and Kharif[9] argued that in order to be valid, a mathematical model has to reproduce the forward-oriented wave fronts which are seen in nature. For this purpose, small nonconservative effects resembling weak wind and weak breaking were added to the otherwise conservative mathematical model based on the Zakharov equation. Shrira, Badulin, and Kharif[9] noted that the simulated patterns exhibit best resemblance with observed patterns when the phase between the Stokes wave train and the perturbation is $-\pi/2$, and this corresponds to a stable equilibrium in their model. In contrast, a conservative modeling lets this phase rotate through all possible values during a cycle of growth and decay of the perturbations, causing the orientation of the crescents to change during the cycle. The model by Shrira, Badulin, and Kharif[9] is also discussed by Dias and Kharif[10] and Craig.[11] Annenkov and Shrira[12,13] also used the Zakharov equation with small nonconservative effects for numerical simulations, but with almost 100 simultaneous perturbations added to the Stokes wave.

Recent, fully nonlinear computations based on conservative modeling have been performed.[14–16] They simulate how inception of class II instability leads to three-dimensional, horseshoe-like structures of finite, large amplitudes. The three-dimensional patterns are usually simulated up to a level where physical breaking of the waves takes place. Fuhrman, Madsen, and Bingham[15] and Fructus, Kharif, Francius, Kristiansen, Clamond, and Grue[16] simulated both the classical horseshoe pattern and the oscillatory ones.

The focus of the present study is to employ a fully nonlinear simulation model to investigate horseshoe patterns on finite water depth. More specifically, the parameter k_0h is of order unity. The model we use (see Sec. II) is the same as Fructus, Kharif, Francius, Kristiansen, Clamond, and Grue[16] used, but they gave only a few preliminary results on finite depth. Apart from these, we know of no other simulations of horseshoe patterns on finite depth. It is, however, important to make such simulations since it is known[7,17] that the five-wave (and higher-order) instabilities dominate in a large range of the possible steepnesses in water of finite depth. An important difference from infinite water depth is that for $k_0h=1$ there exists a region of steepnesses $(0.10<ak_0<0.13)$ where class II is dominating class I and is not leading to breaking. In this region we shall find that the conservative theory leads to a recurrence cycle with a long period (see Sec. III of the paper).

The patterns look significantly different on $k_0h=1$ compared to $k_0h=\infty$. For example, the slopes on the leading and trailing sides of the peaks are nearly equal when $k_0h=1$. The recurrence cycle also looks different on finite depth, since the crests do not flatten out and the peaks do not change transverse position during the cycle. We also report simulations of oscillating horseshoe patterns.

In Sec. IV of the paper, we provide fully nonlinear simulations of six- and seven-wave instabilities. It is, to our knowledge, the first time such higher-order instabilities are numerically simulated. This is especially interesting since Kharif and Francius[17] found that these interactions dominate for sufficiently high steepnesses on small depths. It is explained why the pattern resulting from a six-wave instability on finite depth looks rather like an L_1 horseshoe pattern produced by a five-wave instability on infinite depth. However, the finite-depth property of nearly equal slopes on the leading and trailing sides of the peaks, which was found for five-wave instabilities, applies also for higher-order instabilities.

In Sec. V we discuss combinations of instabilities of different order, focusing on their nonlinear interactions. It is shown that a modulational instability may, by increasing the local steepness, destabilize a three-dimensional (3D) perturbation, so that horseshoe patterns appear. This is in accordance with the hypothesis of Su and Green.[18] Finally, in Sec. VI, we sum up the main results.

II. THE MODEL

We base the current study on simulations made with an efficient fully nonlinear model. The mathematical model is described by Clamond and Grue[19] and Grue[20] and the numerical implementation is described by Fructus, Clamond, Grue, and Kristiansen.[21] Here, we will only briefly outline some characteristics of the method. It is a pseudospectral method which can be seen as a hybrid between an expansion and a boundary integral method. The method has very good stability and accuracy characteristics. Simulations are continued up to a point shortly before physical breaking, where numerical blowup occurs. A test of accuracy and convergence is provided in Appendix B.

The horizontal coordinates are x (chosen here to be in the direction of the Stokes wave propagation) and y, and the vertical coordinate is z, pointing upward from the mean surface elevation. The kinematic and dynamic surface boundary conditions are written in terms of the surface elevation $\eta(x,y,t)$, the surface potential $\tilde{\phi}(x,y,t) \equiv \phi[x,y,\eta(x,y,t),t]$, and $V \equiv \phi_n\sqrt{1+|\nabla\eta|^2}$, where ϕ_n denotes the normal velocity of the free surface and $\nabla = \mathbf{i}\partial/\partial x + \mathbf{j}\partial/\partial y$ the horizontal gradient. Green's theorem is applied to find V as a function of η and $\tilde{\phi}$.

The integral equation resulting from Green's theorem is inverted using Fourier transforms. The kernels of the integrals are partially expanded around the mean surface elevation. In this way, the leading orders are computed very efficiently and globally in the wave field with fast Fourier transforms (FFTs). The remainders of the integrals are then evaluated via quadrature. These are strongly truncated because the kernels are decaying very rapidly in space. This makes the method much more efficient than traditional boundary integral methods. The equation for the Fourier transform of V is given in Appendix A. Using the analytical expression for V, the prognostic equations for η and $\tilde{\phi}$ are stepped forward in time.

The formulation is partially implicit in V,[19] so an iterative solution procedure is applied on the implicit terms. So formally, to be fully nonlinear, the method would need to have an infinite number of iterations. However, one iteration is often enough, making the method explicit. Most of the simulations reported here have been performed with one iteration, and this is normally sufficient to give a very good accuracy (see Appendix B).

The resolution which we have found to be sufficient for this kind of problem is 48 points per wavelength in the longitudinal direction of the Stokes wave (except for the seven-wave interaction presented in Fig. 12 where 64 points per wavelength are used). Thirty-two points are used per crescent wave in the transverse direction. The remainder integrals are usually computed on a domain $[-\lambda_S/2,\lambda_S/2]\times[-\lambda_c/4,\lambda_c/4]$, where λ_S is the wavelength of the Stokes wave and λ_c is the width of a crescent wave, i.e., the transverse wavelength of the perturbation.

The unperturbed Stokes waves of steepness ak_0 on water depth k_0h are computed using a method developed by Fenton.[22] It has been tested that these unperturbed Stokes wave solutions preserve their shape, phase, and energy very well in our model. Perturbations are added in the initial condition in order to look at the instabilities of the finite-depth Stokes wave. The perturbations with wavenumbers k_x and k_y have the following form:

$$\eta' = \epsilon a \sin(k_x x)\cos(k_y y), \tag{1}$$

$$\tilde{\phi}' = -\epsilon a \cos(k_x x)\cos(k_y y)\frac{\cosh[k(\eta+h)]}{\sinh(kh)}\sqrt{\frac{\tanh(kh)}{k}}, \tag{2}$$

where $\epsilon \ll 1$ and $k=\sqrt{k_x^2+k_y^2}$, where $k_x=(1+p)k_0$ and $k_y=qk_0$, k_0 being the wavenumber of the carrier wave. This is just a linear wave solution in the x direction multiplied by a cosine transverse variation. This is the finite-depth version of the perturbation used by Xue, Xü, Liu, and Yue.[14]

Some figures in this paper [Figs. 5(a), 7(a), 14, and 16] show the temporal evolution of the Fourier amplitudes of perturbations, normalized with the initial amplitude of the primary component of the Stokes wave. These show the amplitudes of the components with one sign of k_y, say positive. But there will also be an equally strong component with the opposite sign of k_y. When $k_y \neq 0$, the perturbation with amplitude ϵa will have two components with opposite sign of k_y and with amplitude $\epsilon a/2$. Therefore, the initial value in these figures with normalized Fourier amplitudes will be $\epsilon/2$.

III. FIVE-WAVE INSTABILITIES ON FINITE DEPTH

McLean, Ma, Martin, Saffman, and Yuen[5] and McLean[6,7] divided instabilities of Stokes waves into two classes based on their linear resonance conditions:

$$\text{Class I: } \boldsymbol{k}_1+\boldsymbol{k}_2=N\boldsymbol{k}_0; \quad \omega_1+\omega_2=N\omega_0, \quad N\geqslant 2 \text{ even}, \tag{3}$$

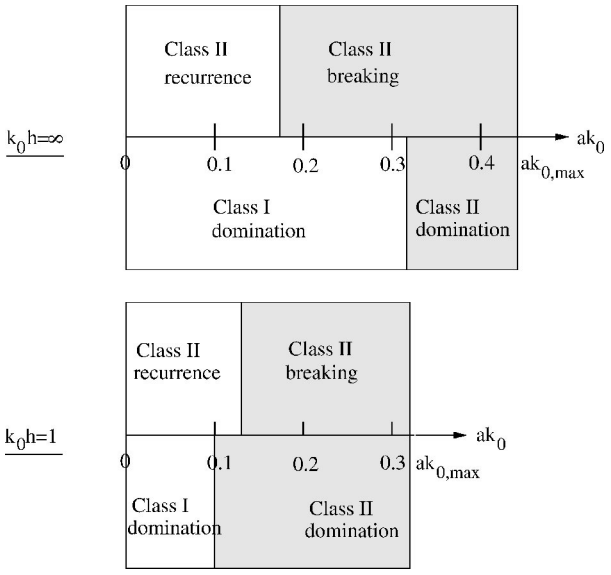

FIG. 1. Threshold steepnesses between class I and class II predominances and between class II recurrence and breaking.

$$\text{Class II: } \boldsymbol{k}_1 + \boldsymbol{k}_2 = N\boldsymbol{k}_0; \quad \omega_1 + \omega_2 = N\omega_0, \quad N \geqslant 3 \text{ odd}, \tag{4}$$

where $\boldsymbol{k}_1$ and $\boldsymbol{k}_2$ are the perturbation wavenumbers and ω_1 and ω_2 are their angular frequencies, while $\boldsymbol{k}_0$ is the wavenumber of the carrier wave and ω_0 its angular frequency. $N=3$ corresponds to five-wave resonances.

Unstable perturbations of Stokes waves of sufficiently large steepness lead to breaking, whereas perturbations on those with sufficiently small steepness lead to recurrence. In the intermediate interval of steepnesses, we observe, as expected, that the fate of the perturbation varies within the instability band, i.e., depends on k_x and k_y. We can define a critical steepness $ak_{0,\mathrm{crit}}$ below which the fastest growing instability will be recurrent and above which it will break. This $ak_{0,\mathrm{crit}}$ will depend on the depth. Fructus, Kharif, Francius, Kristiansen, Clamond, and Grue[16] reported $ak_{0,\mathrm{crit}}(k_0h=\infty) \simeq 0.17$ and $ak_{0,\mathrm{crit}}(k_0h=1) \simeq 0.13$. Figure 1 illustrates this critical steepness at $k_0h=1$ and $k_0h=\infty$ together with the distinction between class I and class II dominances at the same depths. At $k_0h=1$, class II dominates in a large range of steepness, and recurrence is possible within this range.

The case of growth until breaking will be discussed in Sec. III A, recurrence in Sec. III B, and oscillating patterns will be discussed in Sec. III C.

A. Instabilities leading to breaking

Our method does not simulate physical breaking, but when a perturbation grows and approaches the point where breaking occurs, the upper part of the spectrum is lifted. Close to the point of physical breaking (see Appendix B), the spectrum is lifted so much that numerical noise appears, and we stop our simulations.

A pronounced change in the pattern occurs as k_0h is decreased from infinity to $O(1)$. To compare patterns at different depths, we compute steady (phase- locked) perturbations giving L_2 patterns. These are shown in Fig. 2. In the simulations, the steepness is 50% of the maximum steepness for a Stokes wave at a given depth. We will point out three important differences in the wave pattern at $k_0h=1$ compared to $k_0h=\infty$.

First, an important characteristic of the horseshoe pattern on deep water is the front-back asymmetry. For example, the front slopes of the tall waves are steeper than their rear slopes.[2,1,9] On $k_0h=1$, there is still front-back asymmetry since the pattern is not symmetric about the carrier wave crest, but the slopes on the front and rear sides of the peaks are nearly equally steep. This is shown in Fig. 3 which gives $\eta(x)$ and $\partial\eta/\partial x$ in a longitudinal cross section for both depths.

Secondly, our simulations show that the Fourier amplitude of the perturbation is usually allowed to grow larger for finite depth than for infinite depth before wave breaking occurs. For example, it is roughly 50% larger in Fig. 2(a) than in Fig. 2(b). The Fourier amplitude of the perturbation deter-

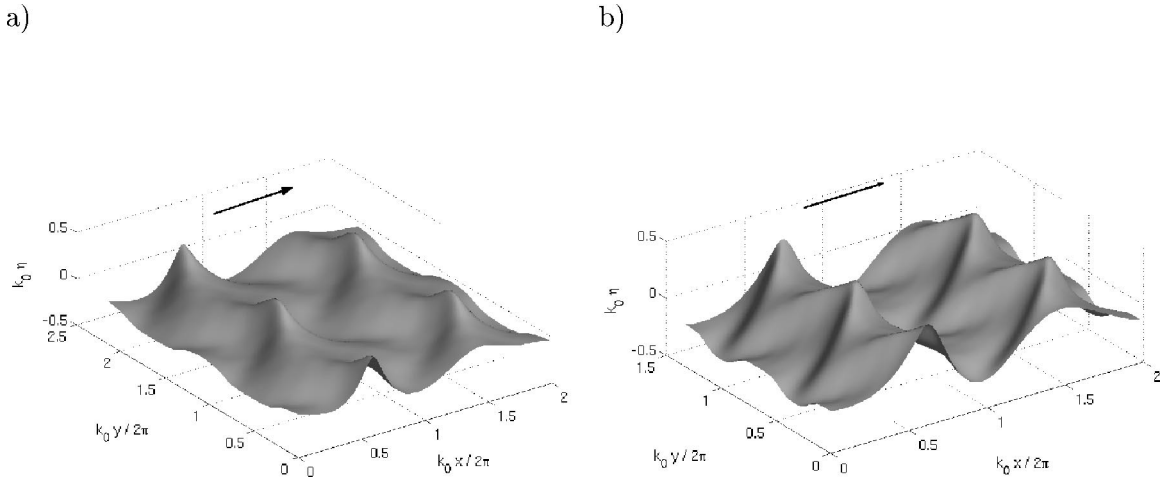

FIG. 2. Crescent waves on finite and infinite depths. (a) $k_0h=1$, $ak_0=0.16$ (=half the critical steepness) shortly before breaking ($t=46.5$ T). The instability at $(k_x,k_y)=(1.5,0.92)k_0$ is triggered with $\epsilon=0.05$. (b) $k_0h=\infty$, $ak_0=0.22$ (=half the critical steepness) shortly before breaking ($t=56.5$ T). The instability at $(k_x,k_y)=(1.5,1.49)k_0$ is triggered with $\epsilon=0.05$.

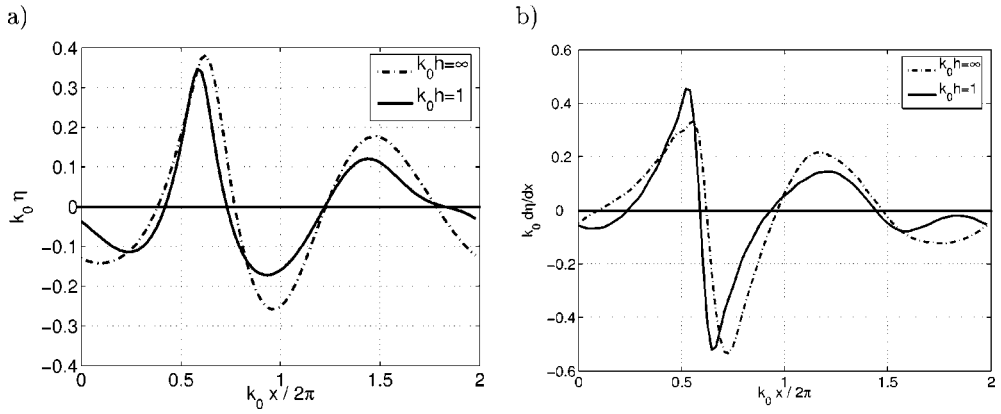

FIG. 3. (a) $\eta(x)$ in a longitudinal cross section in the center of Figs. 2(a) and 2(b). (b) $\partial\eta/\partial x$ in a longitudinal cross section in the center of Figs. 2(a) and 2(b).

mines the ratio between the elevations at the peaks and depressions on the carrier wave crest. Therefore, the peaks are taller relative to the depressions on the carrier wave crest in Fig. 2(a) than in Fig. 2(b).

Thirdly, the region on the trailing side of the carrier wave crest is different on $k_0h=1$ compared to $k_0h=\infty$. For $k_0h=1$, it is a smooth, almost conical, shape between each peak [see Fig. 2(a)]. The curvature of this shape is such that the convex side is looking opposite to the direction of propagation. When the vertical scale is magnified, this appears as the dominating curvature in the pattern. On $k_0h=\infty$, the region on the trailing side of the carrier wave crest is wedge shaped between each peak [see Fig. 2(b)]. This adds definition to the overall crescent shape, which has its convex side looking in the direction of propagation.

To help understanding the patterns, we make sketches like the ones in Fig. 4 showing the carrier and perturbation wave crests. The crossings of the perturbation wave crests with positive and negative k_y are marked with open circles, and we call these points perturbation peaks. The largest peaks in the total wave pattern are located between each carrier wave crest and the closest perturbation peaks. These primary peaks are marked with filled circles. The difference in the region on the trailing side of the carrier wave crest (wedge shape or smooth, conical) is partially due to the angle θ in Fig. 4, given by $\tan\theta=\lambda_x/\lambda_y=k_y/k_x=q/(1+p)$. This angle is smaller for finite depth, since the instability bands are then lower down in the McLean diagrams, corresponding to lower q (larger transverse wavelength). With such a smaller angle, a smooth, conical region can be formed, whereas for a larger angle, a sharper wedge can be formed. The small angle is exemplified in Figs. 2(a) and 4(a) ($\theta=32°$), while the large angle is exemplified in Figs. 2(b) and 4(b) ($\theta=45°$). However, the higher harmonics of the carrier and perturbation waves also play an important, but more complicated, role in the patterns.

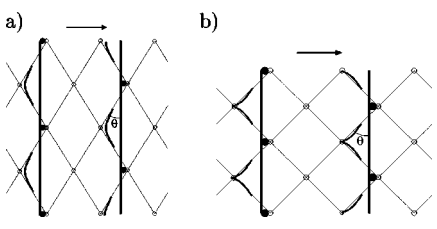

FIG. 4. Schematic drawing of the steady L_2 pattern for five-wave interactions, corresponding to Figs. 2(a) and 2(b). The straight thick lines are carrier wave crests and the thin lines are perturbation wave crests (with positive and negative k_y). Primary peaks are shown with filled circles, perturbation peaks with smaller, open circles. The bold curves are caricatures of the regions on the trailing side of the carrier wave crest. (a) Small $\theta(=32°)$ and (b) large $\theta(=45°)$.

On infinite depth, our simulations show that the peaks sometimes start to flatten out or split in two, like in the middle of a recurrence cycle (see Sec. III B), before breaking occurs. We often see this for perturbations in the upper part of the instability band on infinite depth. However, we have not seen this behavior for $k_0h=1$. This is not surprising since the recurrence cycle is different on $k_0h=\infty$ and $k_0h=1$, as we will see in the following section.

B. Instabilities leading to recurrence

Based on analytical analysis, a wave field composed of a Stokes wave and the two most unstable class II disturbances has been found to undergo "a kind of Fermi–Pasta–Ulam recurrence,"[23] like class I may do. We found that the recurrence cycle is qualitatively different on finite depth than on infinite depth. To be able to point out the differences, we first look at the recurrence cycle on infinite depth, which has been studied before.[8,9,12,16] Figure 5 shows the cycle of the Fourier amplitude of the perturbation and the relative phase between the carrier and the perturbation ($\Phi=3\alpha-2\beta$, where $-\alpha$ and $-\beta$ are the phases of the carrier wave and perturbation, respectively.[9,12]). The development of the Fourier amplitude and $\sin(\Phi)$ closely resembles what was found, e.g., by Annenkov and Shrira.[12] Figure 6 shows the surface elevation at different times. At the beginning, a regular horseshoe pattern develops [see Fig. 6(b)]. The relative phase Φ is such that each carrier wave crest is just slightly behind a row of perturbation peaks (as in Fig. 4). At the point in the cycle where the perturbation has grown to its largest, Φ passes through $-\pi$, which means that each carrier wave crest is in the middle between two rows of perturbation peaks. At this point, the total wave field has flat zigzagging crests, as seen in Fig. 6(c). In the decaying part of the cycle, Φ has rotated into a value corresponding to each carrier wave crest lying

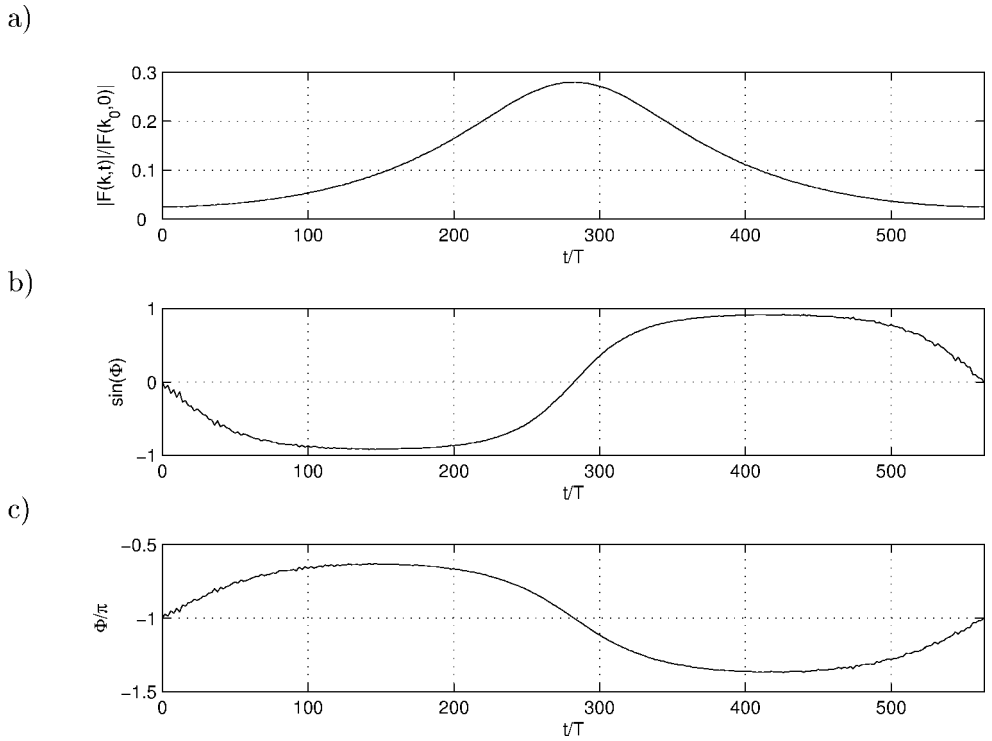

FIG. 5. Temporal evolution of Fourier amplitude and phase during a recurrence cycle on infinite depth. $ak_0=0.15$. The instability at $(k_x,k_y)=(1.5,1.605)k_0$ is triggered with $\epsilon=0.05$. (a) Time dependency of normalized Fourier amplitude of the perturbation. (b) $\sin[\Phi(t)]$. See text for definition of Φ. (c) $\Phi(t)$.

just *in front* of a row of perturbation peaks. This yields inverted horseshoe patterns, as depicted in Fig. 6(d). A slightly perturbed Stokes wave is then regained [see Fig. 6(e)] before a new cycle starts.

Figures 7 and 8 show the development in Fourier and physical space for a recurrence cycle on finite depth ($k_0h=1$). The development of the Fourier amplitude and $\sin(\Phi)$ is qualitatively the same as on infinite depth, but Φ has a different behavior, increasing its value with 2π for each cycle rather than oscillating. This gives rise to a different recurrence cycle in the physical space. Figure 8(b) shows a regular finite-depth pattern [Ref. Fig. 2(a)] growing up. In the middle of the cycle, however, $\Phi=0$, so that each carrier wave crest is on top of a row of perturbation peaks. This yields a total wave field with large primary peaks, and bifurcated crests between them [see Fig. 8(c)]. In the decaying part of the cycle, each carrier wave crest is just in front of a row of perturbation peaks, yielding an inverted horseshoe pattern [see Fig. 8(d)]. At the end of the cycle, a slightly perturbed Stokes wave is regained [see Fig. 8(e)], but $\Phi=\pi$ at this point, rather than $-\pi$ as it was initially. In contrast with the infinite-depth case, the primary peaks maintained their transverse position throughout the cycle. Each cycle will, however, have a transverse shift of these peaks (of half a crescent width) relative to the previous. On infinite depth, in contrast, each cycle is equal.

There are a couple of comments to be made, which applies to both finite and infinite depths. First, there is a forward phase shift in the Stokes wave for each recurrence cycle (about one-third of the Stokes wavelength in these examples). This is because, when the perturbations have grown large, the entire phase-locked system has a larger celerity than the Stokes wave. This may be due to amplitude dispersion.

Secondly, the horseshoe patterns are not oriented the same way throughout the cycle, and this caused Shrira, Badulin, and Kharif[9] to suggest that nonconservative effects were important to keep the orientation of the horseshoes as they are experimentally observed. However, it is important to remember that the time scales for recurrence are very long, in the order of hundreds of fundamental periods, which is more than what is usually observed in experiments. Therefore, the patterns are usually observed in the growing phase of a recurrence cycle, where the convex side is in the direction of the propagation for infinite depth. Also, Fructus, Kharif, Francius, Kristiansen, Clamond, and Grue[16] and the results presented here show that recurrence only occurs below some threshold steepness of the initial Stokes wave. There may, however, be some quasirecurrent behavior after wave breaking, but this is not possible to simulate with our method.

Xue, Xü, Liu, and Yue[14] and Fuhrman, Madsen, and Bingham[15] found that horseshoe patterns could appear without dissipation, and contradicted Shrira, Badulin, and Kharif.[9] However, one should note that Shrira, Badulin, and Kharif[9] never disputed that the patterns could appear without dissipation in the growing phase, but included dissipation in order to avoid the reversed patterns which are not observed. We claim that this lack of observation simply is due to the length scales of recurrence cycles, therefore making dissipation unnecessary as long as physical breaking does not occur.

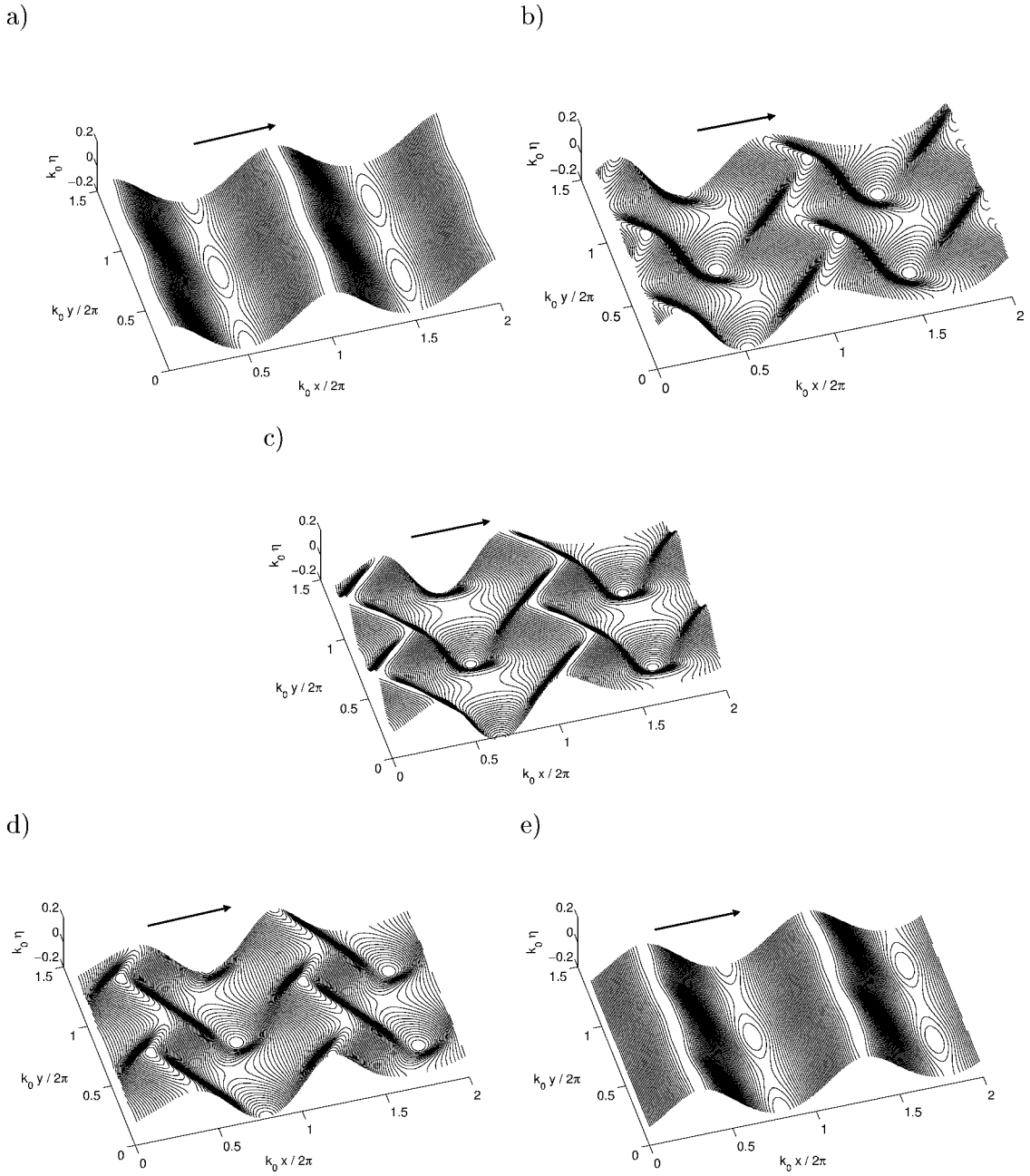

FIG. 6. Temporal evolution of the surface elevation during a recurrence cycle on infinite depth. Parameters as in Fig. 5. (a) $t=0$, (b) $t=220$ T, (c) $t=282$ T, (d) $t=344$ T, and (e) $t=564$ T.

C. Oscillating horseshoe patterns

As for infinite depth, the pattern is steady only for the phase-locked perturbation where $(k_x,k_y)=(1.5,\pm q)k_0$. We have so far been focusing on this particular perturbation, since the highest growth rate is found for this case and since the pattern is steady and simple. Otherwise $(k_x\neq 1.5k_0)$, the peaks oscillate when we follow one carrier wave crest. That is, the peaks appear and disappear, and the transverse position is shifted back and forth for each appearance. For example, the longitudinal periodicity of the pattern is $n\lambda_0$ (L_n pattern) when the perturbation is $(k_x,k_y)=[(1+n)/n,\pm q]k_0$ and $[(2n-1)/n,\mp q]k_0$. An oscillating horseshoe pattern arising from the special nonsteady perturbation $(k_x,k_y)=(1,\pm q)k_0$ and $(2,\mp q)k_0$ is of periodicity L_1 and was observed by Collard and Caulliez.[4]

Oscillating horseshoe patterns are easily simulated on finite depth, too. Figure 9(a) shows an oscillating L_1 horseshoe pattern shortly before breaking for $k_0h=1$ and $ak_0=0.16$. The pattern is rounded in the region on the trailing side of the depressions on the carrier wave crests. This is different from the infinite-depth oscillating horseshoe pattern [Fig. 9(b)], and it is the same difference as we saw for the steady pattern. Also, the Fourier amplitude of the unstable modes are higher in Fig. 9(a) $(k_0h=1)$ than in Fig. 9(b)

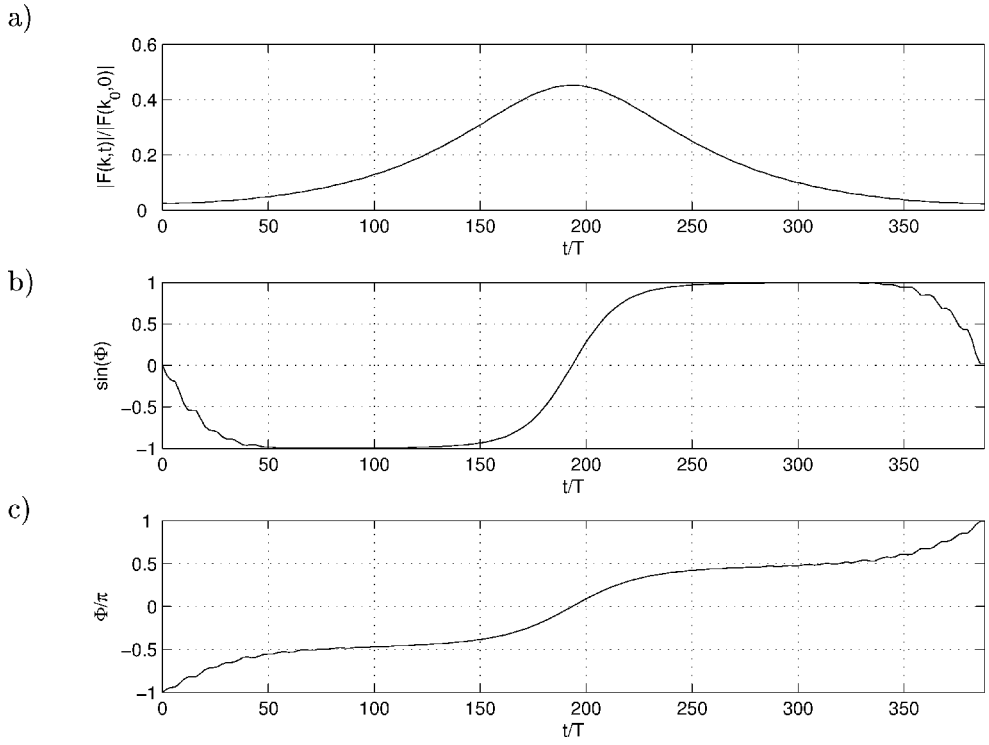

FIG. 7. Temporal evolution of Fourier amplitude and phase during a recurrence cycle on finite depth. $k_0h=1$, $ak_0=0.11$. The instability at $(k_x,k_y)=(1.5,0.98)k_0$ is triggered with $\epsilon=0.05$. (a) Time dependency of normalized Fourier amplitude of the perturbation. (b) $\sin[\Phi(t)]$. See text for definition of Φ. (c) $\Phi(t)$.

$(k_0h=\infty)$. This is the same tendency as we saw for the steady pattern. However, the Fourier amplitudes are not going as high before breaking for the oscillating pattern as for the steady pattern, since there are now four unstable modes $[(1,q)k_0$, $(2,q)k_0$, $(1,-q)k_0$, and $(2,-q)k_0]$ instead of two $[(1.5,q)k_0$ and $(1.5,-q)k_0]$. Again, the slopes on the front and rear sides of the peaks are nearly equally steep on $k_0h=1$. Longitudinal profiles across the peaks are given in Fig. 10(a) and across the lowest part of the crests in Fig. 10(b). We have not succeeded in simulating a purely periodic recurrence cycle of oscillating horseshoe patterns.

The mechanism which selected the oscillatory perturbation in the experiments of Collard and Caulliez,[4] and not the steady perturbation which has a higher growth rate, was reported as enigmatic. Fuhrman, Madsen, and Bingham[15] assumed that the transverse wavenumbers in a tank are limited to the discrete possibilities corresponding to standing waves. If one of these transverse wavenumbers crosses a class II instability band around $p=0$ and $p=1$, but is outside the instability band for $p=0.5$, an oscillating horseshoe pattern will develop. Fructus, Kharif, Francius, Kristiansen, Clamond, and Grue[16] gave a similar explanation, where they considered the possible triggering of those instabilities by parametric resonance.

IV. HIGHER-ORDER INSTABILITIES ON FINITE DEPTH

With our numerical method it is easy to simulate instabilities of higher order than five-wave instabilities. This is an advantage in comparison with methods based on the Zakharov equation, since its kernel for six-wave (and higher) interactions is not computed and would be extremely complicated. An example of a steady pattern resulting from a simulation of a six-wave instability is provided in Fig. 11 $[k_0h=1$, $ak_0=0.20$, and $(k_x,k_y)=(2,2.12)k_0]$.

The most conspicuous difference from a steady pattern produced by a five-wave instability is that the primary peaks in Fig. 11 are aligned. It is easy to explain why the steady pattern resulting from a six-wave interaction is L_1. A steady pattern can be defined as a pattern where the primary peaks follow the Stokes wave crest without changing their transverse position (except in recurrence). A simple geometrical argument shows that this is fulfilled for $\omega/\omega_0=k_x/k_0$ for each of the two perturbations (positive and negative k_y), each having the same angular frequency ω and longitudinal wavenumber k_x. The resonance conditions for this steady pattern are $2k_x=Nk_0$ and $2\omega=N\omega_0$. The first can be written $\lambda_0=N/2\lambda_x$, where λ_x is the longitudinal wavelength of the perturbations. For class I, N is an even number, and $N/2$ is an integer, so the periodicity of the wave pattern is λ_0, which can be called L_1 using Su's notation. For class II, $N/2$ is not an integer, but N is, so $2\lambda_0=n\lambda_x$, and we have an L_2 pattern. Thus, a steady class I pattern is L_1 and a steady class II pattern is L_2.

It is therefore natural to compare the pattern in Fig. 11 with the L_1 oscillating horseshoe patterns in Fig. 9. Figure 11 most closely resembles Fig. 9(b), i.e., the five-wave interaction at *infinite* depth. This may seem surprising since $k_0h=1$ both in Figs. 9(a) and 11, but the angle θ as defined in Sec. III A is 33°, 45°, and 47°, respectively, in Figs. 9(a), 9(b), and 11. This is in agreement with the discussion in Sec.

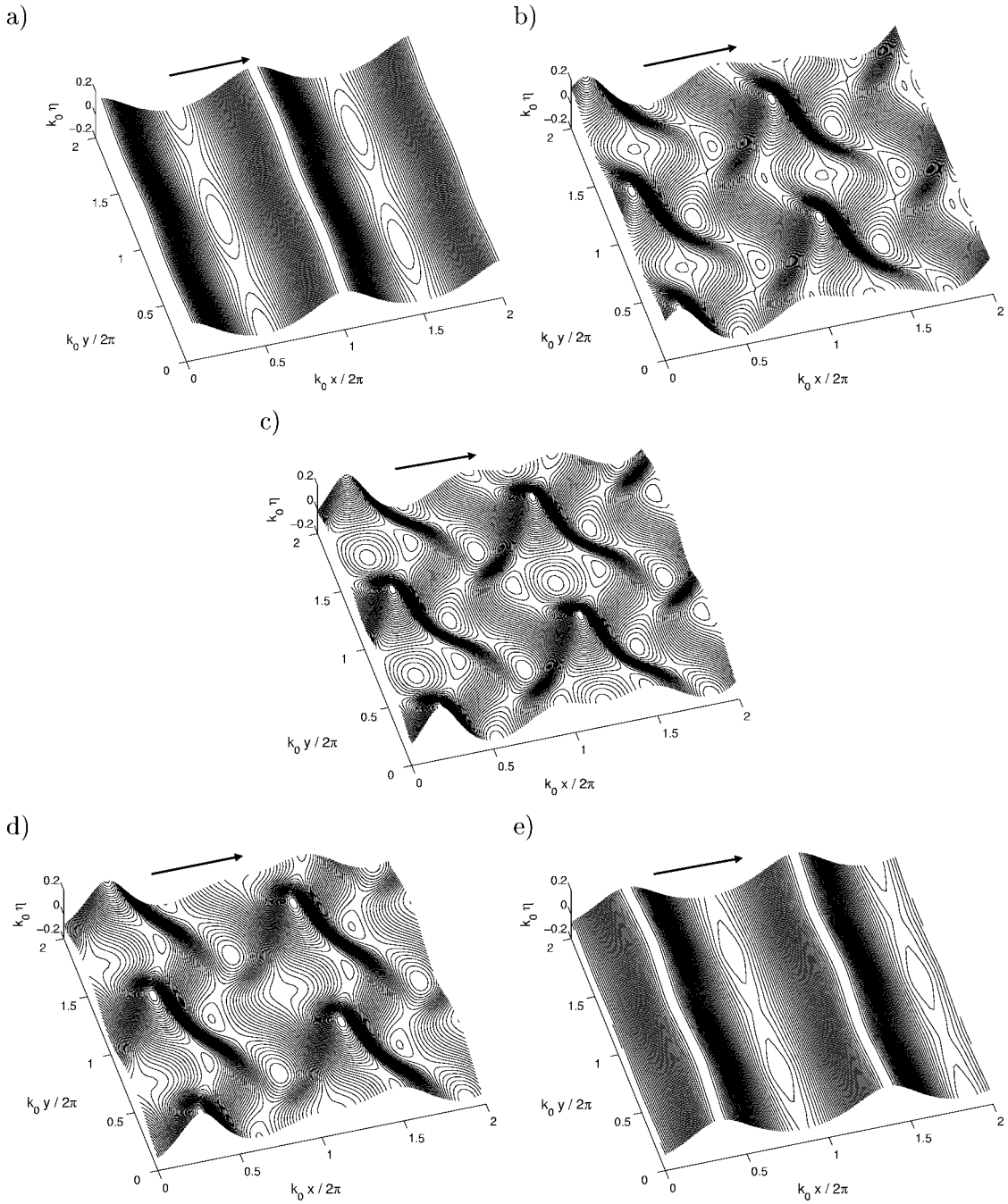

FIG. 8. Temporal evolution of the surface elevation during a recurrence cycle on finite depth. Parameters as in Fig. 7 (a) $t=0$, (b) $t=156$ T, (c) $t=194$ T, (d) $t=232$ T, and (e) $t=388$ T.

III A that θ is an important parameter in characterizing the patterns. However, the difference between the slopes on the front and rear sides of the peaks is small for the finite-depth six-wave interaction. This is the same property as was found for patterns resulting from five-wave interactions on finite depth, in contrast with on infinite depth.

We find it useful to make schematic drawings of the steady patterns resulting from six- and seven-wave interactions in the same way as we did for five-wave interactions. This is provided in Figs. 12(a) and 12(b). Figures 12(c) and 12(d) show the surface elevations of six- and seven-wave instabilities, respectively. $k_0h=0.5$ and $ak_0=0.12$ in both simulations. The fastest growing instability for this depth and steepness is a six-wave interaction.[17] It can easily be seen how the peaks and troughs of the computed wave field corresponds to the schematic drawings.

The higher the order of the resonance, the smaller is the longitudinal distance between two consecutive rows of perturbation peaks relative to the carrier wavelength (i.e., $\lambda_x/\lambda_0=2/N$ decreases as N increases). Therefore, the longitudinal extent of the main crests in the pattern becomes smaller relative to the carrier wavelength when the order of the instability is increased. It is noteworthy that when the depth is decreased and steepness increased, the Stokes wave

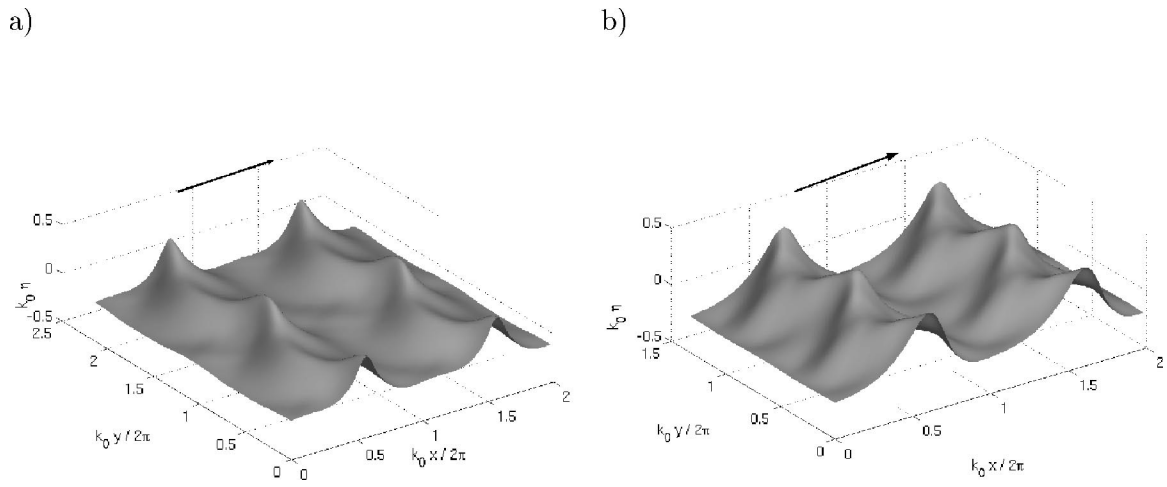

FIG. 9. Oscillating horseshoe patterns on finite and infinite depths. (a) $k_0h=1$, $ak_0=0.16$ (=half the critical steepness) shortly before breaking ($t=53.5$ T). The instability at $(k_x,k_y)=(1.00,0.97)k_0$ is triggered with $\epsilon=0.05$. A convergence test for this particular case is provided in Appendix B. (b) $k_0h=\infty$, $ak_0=0.22$ (=half the critical steepness) shortly before breaking ($t=67.5$ T). The instability at $(k_x,k_y)=(1.00,1.48)k_0$ is triggered with $\epsilon=0.05$.

itself becomes more 'cnoidal,' with narrow peaks and long troughs, and the order of the dominating instability increases. Therefore, the dominating instability "fits" with the Stokes wave profile at the given depth and steepness.

V. COMBINATIONS OF INSTABILITIES OF DIFFERENT ORDER

A. Su and Green's trigger mechanism

Su and Green[18] suggested that two-dimensional class I modulations can trigger class II instabilities. More specifically, the modulation of a Stokes wave with weak or moderate steepness causes sufficiently steep waves in a part of each group to trigger class II instabilities. They based this on experimental observations on deep water. Their suggestion may seem reasonable, since, for weakly nonlinear periodic waves, the steepness is the parameter governing the relative strengths of class I and II instabilities, with higher steepnesses increasing the relative strength of class II.[6,7]

We believe that one way of achieving this trigger mechanism is by choosing a 3D perturbation just below the class II instability band, so that this perturbation alone will be stable. But with a two-dimensional (2D) modulation of the wave train, the steepness will locally be increased. The class II instability band will normally be lowered and widened when the steepness is increased. Therefore, we can expect that the 3D perturbation, which initially was just below the instability band, will after some time be included in the band and hence destabilized.

A simulation is made to verify the possibility of this trigger mechanism. k_0h is set to 1.5 and $ak_0=0.20$. A 3D perturbation just below the class II instability band was excited alone and with a 2D modulation. Figure 13 shows the wave field after 80 periods in both cases. The horseshoe patterns are visible only when a 2D modulation was present, as expected. This clearly shows an example where a class I instability triggers a class II instability.

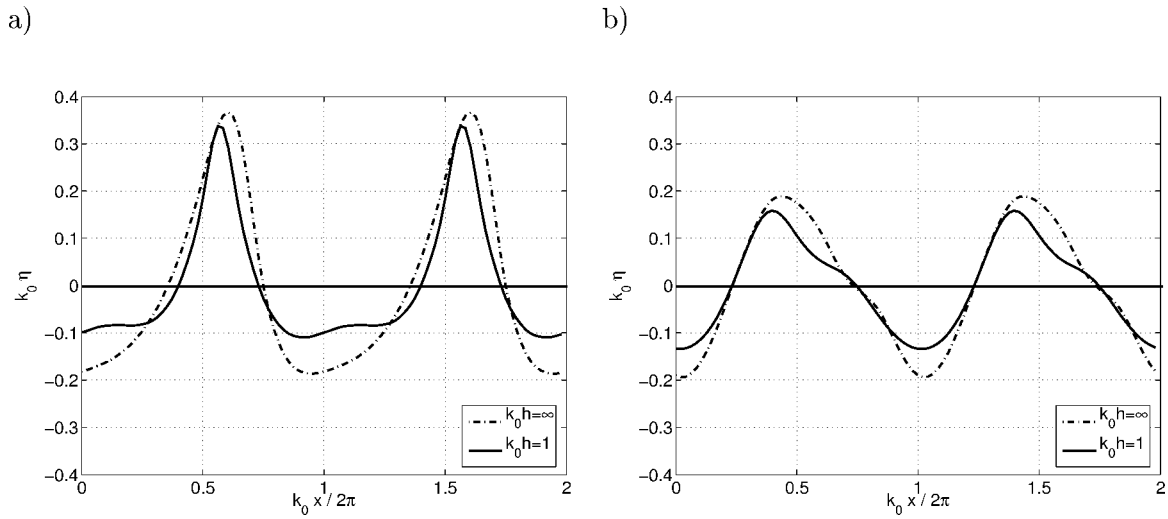

FIG. 10. (a) $\eta(x)$ in a longitudinal cross section in the center of Figs. 9(a) and 9(b). (b) $\eta(x)$ in a longitudinal cross section at $1/4$ of the transverse width of Figs. 9(a) and 9(b).

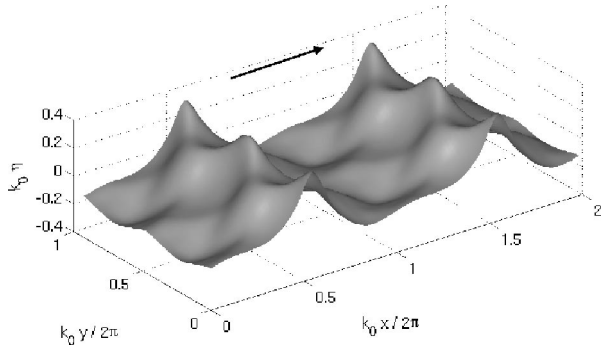

FIG. 11. Six-wave instability with $k_0h=1$, $ak_0=0.20$ at $t=35.5$ T. The instability at $(k_x,k_y)=(2,2.12)k_0$ is triggered with $\epsilon=0.05$.

A few comments are necessary. The effect will be easiest to observe when each crest spends a long time in the steep part of a group, giving sufficient time for a class II instability to grow on it. This favors long groups (seen experimentally in Ref. 24), but also shallow depths, since the phase and group velocities then approach each other. However, for $k_0h<1.36$, the class I instability region has detached from the p axis. Therefore, we chose $k_0h=1.5$. A large steepness will also make the effect more easily observable, since the class II instability will then grow up quickly, which is why we chose $ak_0=0.20$. The perturbation was put at $(k_x,k_y)=(1.3,1.17)k_0$ which is just below the lower limit of the instability band, which is at $k_y=1.20k_0$ for this k_x.

It can be argued that the effect which we tested is a far-fetched one since it relied on a choice of the 3D perturbation just below the class II instability band. However, in a channel experiment, only transverse wavenumbers corresponding to standing waves across the width of the tank are allowed, at least for long-time development. Therefore, it is possible to have an experimental situation where the class II instability band initially lies between two harmonics of the tank width. A 2D modulation may then cause horseshoe patterns to develop.

Fructus, Kharif, Francius, Kristiansen, Clamond, and Grue[16] simulated a different effect. They had a 3D perturbation which was unstable also without the presence of a class I perturbation. However, a recurrent class I perturbation, in its decaying phase, boosted the growth of the class II instability, ultimately leading to breaking. This may be a candidate for an explanation of the observations of Su and Green. Their simulation was made on infinite depth with $ak_0=0.13$.

There has been skepticism to Su and Green's suggested trigger mechanism in the literature. Stiassnie and Shemer,[8] having made simulations using the Zakharov equation, said that their results contradict the hypothesis of the trigger mechanism. They said this because their results indicated that whenever the initial level of class I disturbances is substantially higher than that of class II, class I wave components seem to suppress the 3D (class II) components. In our view, their results do not exclude the possibility of the trigger mechanism, but merely state that the opposite may also be

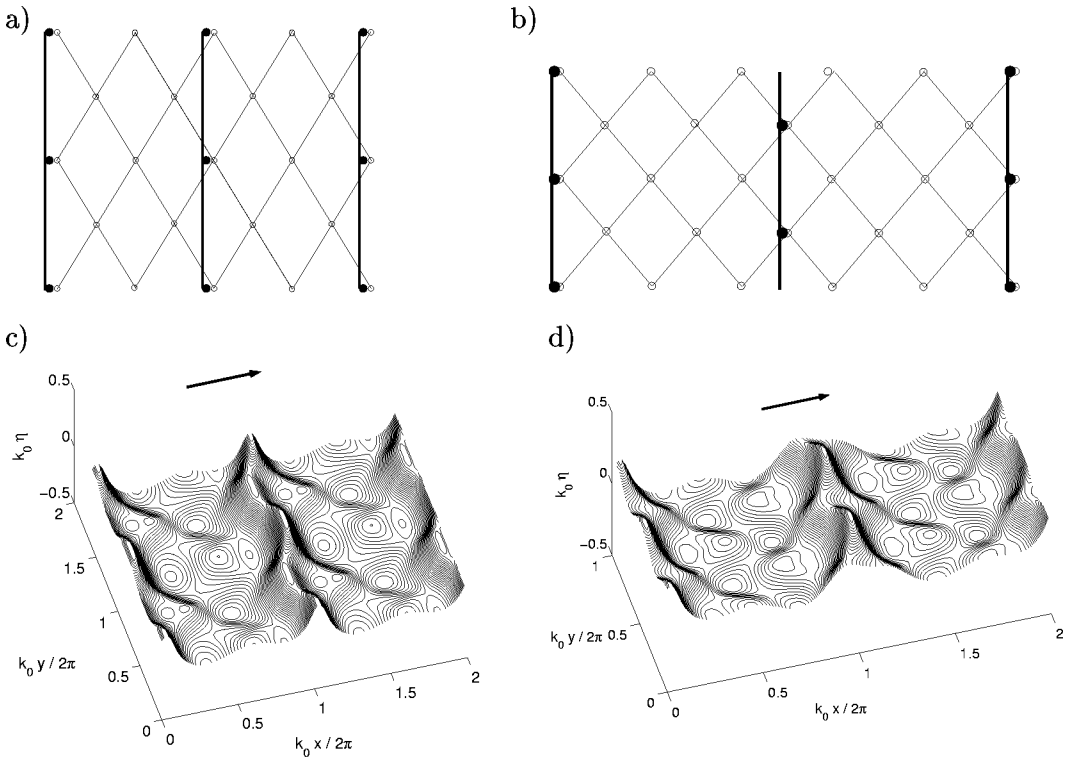

FIG. 12. Six- and seven-wave interactions. (a) Schematic drawing of the steady pattern resulting from a six-wave interaction. See Fig. 4 and text for explanation. (b) Schematic drawing of the steady pattern resulting from a seven-wave interaction. (c) Surface elevation after 24 periods with $k_0h=0.5$, $ak_0=0.12$. The six-wave instability at $(k_x,k_y)=(2,1.24)k_0$ is triggered with $\epsilon=0.05$. (d) Surface elevation after 28 periods with $k_0h=0.5$, $ak_0=0.12$. The seven-wave instability at $(k_x,k_y)=(2.5,2.12)k_0$ is triggered with $\epsilon=0.05$.

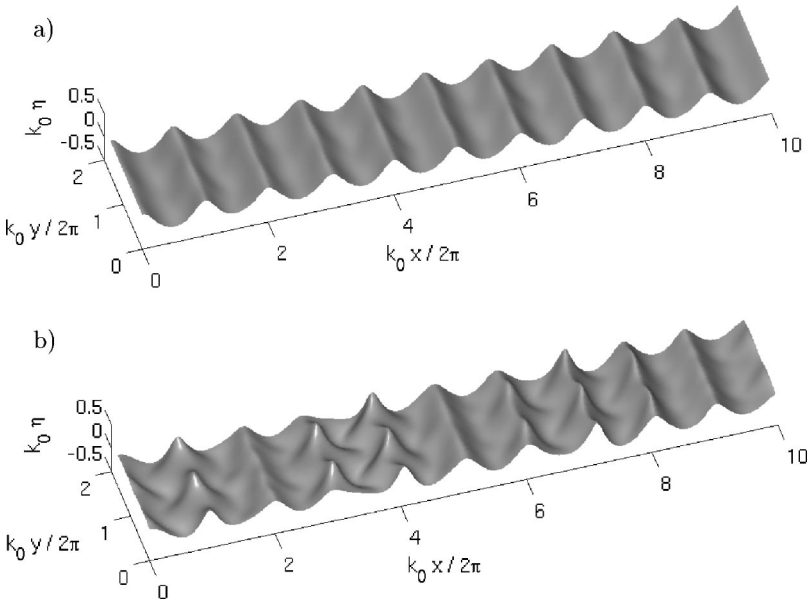

FIG. 13. A 3D perturbation becoming unstable because of the presence of a 2D modulation. $k_0h=1.5$, $ak_0=0.20$. (a) Wave field 80 T after $(k_x,k_y)=(1.30,1.17)k_0$ was triggered alone. (b) Wave field 80 T after both $(k_x,k_y)=(1.30,1.17)k_0$ and $(k_x,k_y)=(1.10,0)k_0$ were triggered. [The width of the computational domain is only one transverse wavelength, but is expanded to two here (since we have periodic boundary conditions) to clarify the patterns.]

the case, i.e., class I suppressing class II. Stiassnie and Shemer also mentioned that one can see from most of their results that significant class II activity initially appears to accompany high levels of class I disturbances. Annenkov and Shrira[12,13] agreed, also based on simulation with the Zakharov equation, with Stiassnie and Shemer in not supporting the trigger mechanism of Su and Green. They also argued analytically that with intense Benjamin–Feir oscillations, the averaged phase of the class II satellites is removed from its optimal value.

We cannot conclude definitely about the explanation of Su and Green's specific experimental observations, but we have seen in numerical simulations that a class I instability may indeed trigger a class II instability.

B. Other interactions between class I and class II

We shall here look at interactions between class I four-wave instabilities and class II five-wave instabilities until breaking occurs. On finite depth, class II generally has growth rates larger or roughly as large as class I. When the class II perturbation is in the regime where it leads to breaking on its own, its growth rate is usually considerably larger than the growth rate of class I perturbations. In those cases, interactions between the two classes are not so interesting since only little time is available for the relatively slow growth of class I before breaking occurs due to class II. Interactions are more interesting for smaller steepnesses when the class II perturbation is in the regime where it leads to recurrence on its own. Then class I has more time to grow and interact with class II.

Figure 14 shows the results from a simulation in this regime. Figure 14(a) shows the development of the class II perturbation when it is the only excited perturbation, and Fig. 14(b) shows the development of the class I perturbation when it is the only excited perturbation. Figure 14(c) shows the development when both class I and II perturbations are excited. It is clear that when the initially dominating class II perturbation is decaying, it is giving away energy to the class I perturbation, thus boosting the latter. After some 160 periods, class I is completely dominating, and in the end, the combination of the perturbations leads to breaking.

The infinite-depth counterpart of this was simulated by Fructus, Kharif, Francius, Kristiansen, Clamond, and Grue.[16] As mentioned above, they reported that on infinite depth, a recurrent class I perturbation may in its decaying phase boost a slower class II perturbation, leading to breaking. On finite depth, classes I and II have shifted roles.

Whenever both class I and class II perturbations are present, we have the following resonance conditions fulfilled:

$$\boldsymbol{k}_1+\boldsymbol{k}_2^*=\boldsymbol{k}_3+\boldsymbol{k}_4^*-\boldsymbol{k}_0, \tag{5}$$

$$\boldsymbol{k}_1^*+\boldsymbol{k}_2=\boldsymbol{k}_3+\boldsymbol{k}_4^*-\boldsymbol{k}_0, \tag{6}$$

$$\boldsymbol{k}_1+\boldsymbol{k}_2^*=\boldsymbol{k}_3^*+\boldsymbol{k}_4-\boldsymbol{k}_0, \tag{7}$$

$$\boldsymbol{k}_1^*+\boldsymbol{k}_2=\boldsymbol{k}_3^*+\boldsymbol{k}_4-\boldsymbol{k}_0, \tag{8}$$

where $\boldsymbol{k}_0$ is the carrier wave vector, $\boldsymbol{k}_1$, $\boldsymbol{k}_1^*$, $\boldsymbol{k}_2$, and $\boldsymbol{k}_2^*$ are the class I perturbation wave vectors (where * indicates negative transverse wavenumber) and similarly, $\boldsymbol{k}_3$, $\boldsymbol{k}_3^*$, $\boldsymbol{k}_4$, and $\boldsymbol{k}_4^*$ are the class II perturbation wave vectors. The corresponding resonance conditions in angular frequency are also approximately fulfilled. This makes the direct interactions between classes I and II possible.

In the simulations reported in Fig. 14, we chose the transverse wavenumber of the class II perturbation to be exactly three times the transverse wavenumber of the class I perturbation. Also, both the excited perturbations had $k_x=1.5$. These choices were made in order to have only two carrier wavelengths in the longitudinal direction and three horseshoes in the transverse direction, since this enabled efficient fully nonlinear computations at a long time scale. However, this configuration also means that other nonlinear couplings may be possible in addition to the ones described above. Even though some resonances are fulfilled in k space,

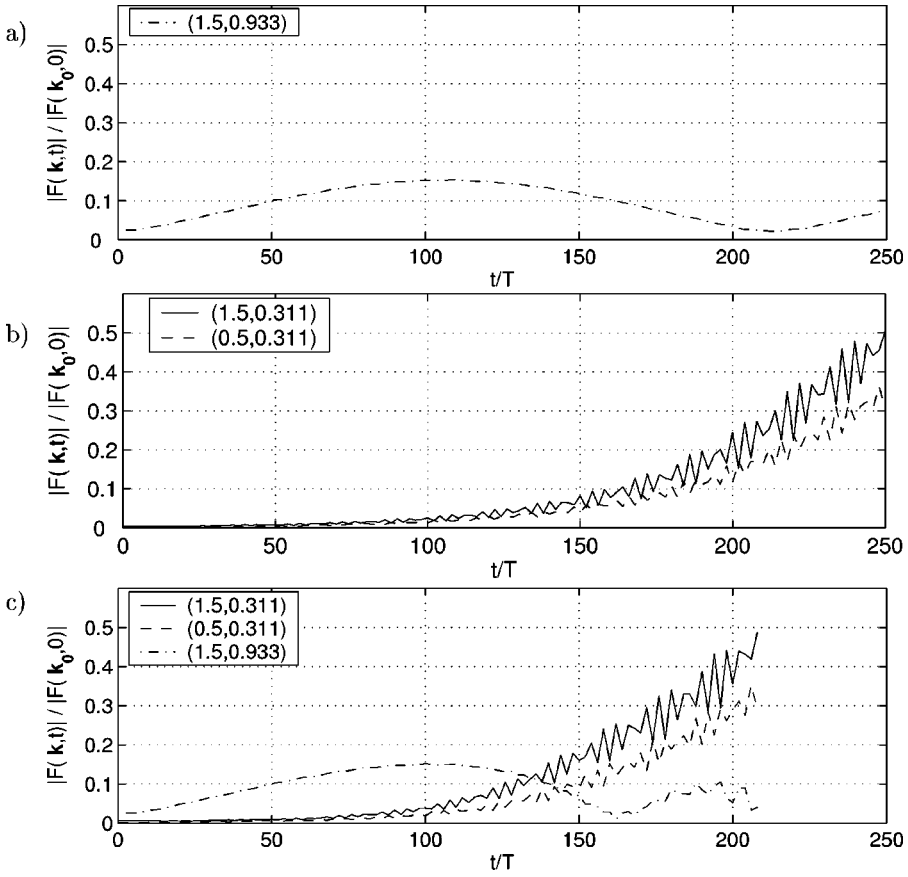

FIG. 14. Class II boosting class I on $k_0h=1$ with $ak_0=0.14$. (a) A class II perturbation at $(k_x,k_y)=(1.5,0.933)k_0$ is triggered alone ($\epsilon=0.05$) giving a recurrent development. (b) A class I perturbation at $(k_x,k_y)=(1.5,0.311)k_0$ is triggered alone ($\epsilon=0.01$) leading to breaking after 250 T. (c) Both perturbations triggered at the same time.

the corresponding angular frequencies do not fulfill the resonances sufficiently well for these couplings to be important.

Having seen that class II can boost class I on finite depth, we turn our attention to the scenario of class I suppressing class II. It has been reported on infinite depth that high levels of class I could suppress class II.[8,12,13,16] Fructus, Kharif, Francius, Kristiansen, Clamond, and Grue[16] simulated this and explained it by class I locally increasing the steepness of the wave train, thus lowering the class II instability band. An initial class II perturbation may then fall out of the instability band. Note that this explanation is the counterpart effect of the one we discussed and demonstrated in Sec. V A where class I destabilized a perturbation which was initially stable. For $k_0h<1.36$, however, the class I instability band has detached from the k_x axis, so 2D modulations which directly modify the local steepness do not occur, so class I do not suppress class II.

Finally, one could suspect that class II may suppress class I when the former is much stronger for high steepnesses at finite depth. This is, however, not observed, since class II does not directly affect any key parameter that governs class I instability in the way that class I is directly affecting the local steepness that governs the class II instability.

VI. SUMMARY OF MAIN RESULTS

We have investigated instabilities of Stokes waves at finite depth. We used a fully nonlinear, accurate, conservative potential formulation model. Five-wave and higher-order instabilities dominate on a large range of steepnesses on finite depth, and these are the focus of our investigation. In particular, there is on finite depth a regime where five-wave interactions dominate, and are recurrent instead of going to breaking. This is a situation especially well suited for a conservative model. We also made simulations in the regime where five-wave instabilities lead to breaking. In both regimes, the patterns are considerably different for $k_0h=1$ as compared to $k_0h=\infty$. For example, in the phase where the perturbations are growing, the slopes on the leading and trailing sides of the peaks are nearly equal for $k_0h=1$. After the growing phase, either breaking or recurrence occurs. In the case of recurrence with $k_0h=1$, the crests do not flatten out and the peaks do not shift transversal position as they do for $k_0h=\infty$.

Higher-order instabilities are described, and for the first time they are numerically simulated. They are exemplified here by steady L_1 patterns resulting from six-wave instabilities and a steady L_2 pattern resulting from a seven-wave instability. Further, simulations show that a 2D class I (four-wave) perturbation can destabilize a 3D perturbation so that a class II (five-wave) instability grows. This is in accordance with the hypothesis of Su and Green.[18] Finally, a recurrent class II interaction may boost a class I interaction.

ACKNOWLEDGMENTS

This work has been funded by the Norwegian Research Council through the strategic university program "Modeling of currents and waves for sea structures." We are also grateful to Dr. Karsten Trulsen for discussions and comments.

APPENDIX A: BOUNDARY INTEGRALS WITH FINITE DEPTH

The model is described by Grue[20] and in detail with implementation by Fructus, Clamond, Grue, and Kristiansen,[21] but we give here the boundary integrals with finite depth. We use Green's theorem to express $V \equiv \phi_n\sqrt{1+|\nabla\eta|^2}$ as a function of η and $\tilde{\phi}$. Green's theorem can be used as follows:

$$\int_S \left(\frac{1}{r}+\frac{1}{r_B}\right)\frac{\partial\phi'}{\partial n'}dS' = 2\pi\tilde{\phi} + \int_S \tilde{\phi}'\frac{\partial}{\partial n}\left(\frac{1}{r}+\frac{1}{r_B}\right)\mathrm{d}S',$$

where $\tilde{\phi}=\tilde{\phi}(x,y,t)$, $\tilde{\phi}'=\tilde{\phi}(x',y',t)$, $r^2=R^2+(z'-z)^2$, $r_B^2=R^2+(z'+z+2h)^2$, $R=|(x',y')-(x,y)|$, and S is the free surface with $\mathrm{d}S'=\sqrt{1+|\nabla'\eta'|^2}\mathrm{d}x'\mathrm{d}y'$. We then introduce $D=(\eta'-\eta)/R$ and $D_B=(\eta'+\eta)/R_B$, where $R_B^2=R^2+4h^2$. The variables D and D_B are exploited to deduce the leading behavior of the integral equation. This is inverted analytically by means of a Fourier transform. Integrals involved are

$$\mathcal{F}\{R^{-1}\} = 2\pi k^{-1}e^{-i\mathbf{k}\cdot\mathbf{x}'}, \quad \mathbf{x}' \equiv (x',y'),$$

$$\mathcal{F}\{R_B^{-1}\} = 2\pi e_h k^{-1}e^{-i\mathbf{k}\cdot\mathbf{x}'}, \quad e_h \equiv e^{-2kh},$$

where $\mathcal{F}$ denotes the Fourier transform ($\iint_{-\infty}^{\infty}e^{-i\mathbf{k}\cdot\mathbf{x}}\mathrm{d}\mathbf{x}$). The remainders are calculated with numerical integration. These integrals have kernels which are decaying fast and can therefore be quickly truncated. After some algebra one obtains

$$\begin{aligned}\mathfrak{F}(V) = {} & k\tanh(kh)\mathcal{F}(\tilde{\phi}) - k\tanh(kh)\mathfrak{F}\{\eta V_1\} \\ & - i\mathbf{k}\cdot\mathfrak{F}\{\eta\nabla\tilde{\phi}\} + kC_h[e_h\mathcal{F}[\eta(V-V_1)] \\ & + \mathcal{F}(\eta\mathcal{F}^{-1}[e_h\mathcal{F}(V-V_1)])] + kC_h\{\mathcal{F}[T(\tilde{\phi}) \\ & + T_B(\tilde{\phi})] + \mathcal{F}[N(V)+N_B(V)]\},\end{aligned} \tag{A1}$$

where $V_1=\mathfrak{F}^{-1}[k\tanh(kh)\mathfrak{F}(\tilde{\phi})]$, $C_h\equiv 1/(1+e_h)$, and

$$T(\tilde{\phi}) = \frac{1}{2\pi}\int\int_{-\infty}^{\infty}\tilde{\phi}'[1-(1+D^2)^{-3/2}]\nabla'\left[(\eta' - \eta)\nabla'\frac{1}{R}\right]\mathrm{d}\mathbf{x}', \tag{A2}$$

$$N(V) = \frac{1}{2\pi}\int\int_{-\infty}^{\infty}\frac{V'}{R}[1-(1+D^2)^{-1/2}]\mathrm{d}\mathbf{x}', \tag{A3}$$

$$\begin{aligned}= {} & \frac{1}{2\pi}\int\int_{-\infty}^{\infty}\frac{V'}{R}[1-(1+D^2)^{-1/2}-D^2/2]\mathrm{d}\mathbf{x}' \\ & + \mathcal{F}^{-1}\left[\frac{1}{2}\mathcal{F}(2\eta\mathcal{F}^{-1}[k\mathcal{F}(\eta V)]) - \frac{k}{2}\mathcal{F}(\eta^2 V) \right. \\ & \left. - \frac{1}{2}\mathcal{F}(\eta^2 F^{-1}[k\mathcal{F}(V)])\right],\end{aligned} \tag{A4}$$

$$T_B(\tilde{\phi}) = -\frac{1}{2\pi}\int\int_{-\infty}^{\infty}\tilde{\phi}'\frac{12h^2(\eta'+\eta)}{R_B^5}\mathrm{d}\mathbf{x}' + \frac{1}{2\pi}\int\int_{-\infty}^{\infty}\tilde{\phi}'[\boldsymbol{R}\cdot\nabla'\eta' - (\eta'+\eta) - 2h]\left[\frac{1}{r_B^3}-\frac{1}{R_B^3}\right]\mathrm{d}\mathbf{x}', \tag{A5}$$

$$\begin{aligned}= {} & -\frac{1}{2\pi}\int\int_{-\infty}^{\infty}\tilde{\phi}'\left(\frac{280h^4}{R_B^2}-30h^2\right)\frac{(\eta'+\eta)^3}{R_B^7}\mathrm{d}\mathbf{x}' + \frac{1}{2\pi}\int\int_{-\infty}^{\infty}\tilde{\phi}'[\boldsymbol{R}\cdot\nabla'\eta' - (\eta'+\eta) - 2h]\cdot\left[\frac{1}{r_B^3}-\frac{1}{R_B^3}+\frac{6h(\eta'+\eta)}{R_B^5}\right. \\ & \left. - \left(\frac{30h^2}{R_B^2}-\frac{3}{2}\right)\frac{(\eta'+\eta)^2}{R_B^5}\right]\mathrm{d}\mathbf{x}' + \mathcal{F}^{-1}\left[\frac{1}{2}e_h i\mathbf{k}\cdot\mathcal{F}(\eta^2\nabla\tilde{\phi}) + \frac{1}{2}\mathcal{F}(2\eta\mathcal{F}^{-1}[e_h i\mathbf{k}\cdot\mathcal{F}(\eta\nabla\tilde{\phi})]) - \frac{1}{2}\mathcal{F}(\eta^2\mathcal{F}^{-1}[e_h k^2\mathcal{F}(\tilde{\phi})])\right. \\ & \left. - \frac{k}{6}e_h i\mathbf{k}\cdot\mathcal{F}(\eta^3\nabla\tilde{\phi}) - \frac{1}{6}\mathcal{F}(3\eta\mathcal{F}^{-1}[e_h ki\mathbf{k}\cdot\mathcal{F}(\eta^2\nabla\tilde{\phi})]) - \frac{1}{6}\mathcal{F}(3\eta^2 F^{-1}[e_h ki\mathbf{k}\cdot\mathcal{F}(\eta\nabla\tilde{\phi})]) + \frac{1}{6}\mathcal{F}(\eta^3\mathcal{F}^{-1}[e_h k^3\mathcal{F}(\tilde{\phi})])\right],\end{aligned} \tag{A6}$$

$$N_B(V) = \frac{1}{2\pi}\int\int_{-\infty}^{\infty}V'\left[\frac{1}{R_B}-\frac{2h(\eta'+\eta)}{R_B^3}-\frac{1}{r_B}\right]\mathrm{d}\mathbf{x}', \tag{A7}$$

$$\begin{aligned}= {} & \frac{1}{2\pi}\int\int_{-\infty}^{\infty}V'\left[\frac{1}{R_B}-\frac{2h(\eta'+\eta)}{R_B^3}-\frac{1}{r_B}\right]\mathrm{d}\mathbf{x}' + \frac{1}{2\pi}\int\int_{-\infty}^{\infty}V'\left[\left(\frac{6h^2}{R_B^2}-\frac{1}{2}\right)\frac{(\eta'+\eta)^2}{R_B^3} - \left(\frac{20h^3}{R_B^2}-3h\right)\frac{(\eta'+\eta)^3}{R_B^5}\right]\mathrm{d}\mathbf{x}' \\ & + \mathcal{F}^{-1}\left[-\frac{k}{2}e_h\mathcal{F}(\eta^2 V) - \frac{1}{2}\mathcal{F}(2\eta F^{-1}[ke_h\mathcal{F}(\eta V)]) - \frac{1}{2}\mathcal{F}(\eta^2 F^{-1}[ke_h\mathcal{F}(V)]) + \frac{k^2}{6}e_h\mathcal{F}(\eta^3 V) + \frac{1}{6}\mathcal{F}(3\eta\mathcal{F}^{-1}[e_h k^2\mathcal{F}(\eta^2 V)])\right. \\ & \left. + \frac{1}{6}\mathcal{F}(3\eta^2\mathcal{F}^{-1}[e_h k^2\mathcal{F}(\eta V)]) + \frac{1}{6}\mathcal{F}(\eta^3\mathcal{F}^{-1}[e_h k^2\mathcal{F}(V)])\right].\end{aligned} \tag{A8}$$

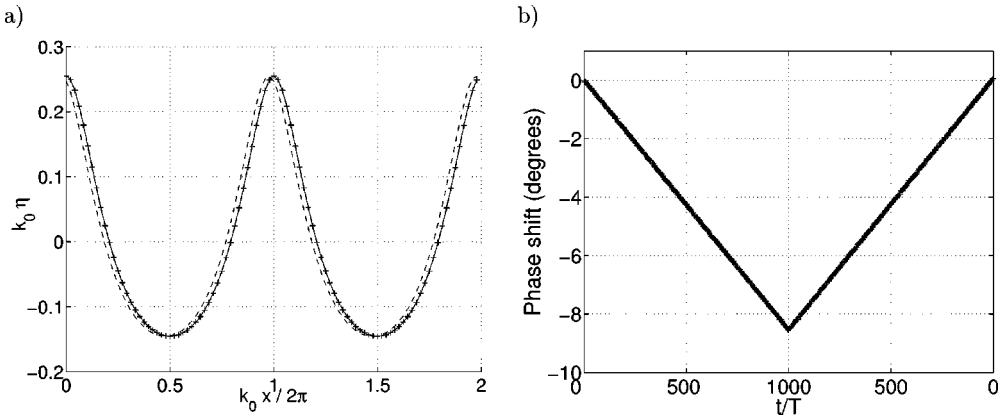

FIG. 15. (a) Profile of a Stokes wave [$k_0h=1$ ($\lambda/h=6.28$), $ak_0=0.20$ ($a/h=0.2$)] at $t=0$ ($-$), after 1000 periods ($--$), and at $t=0$ ($+$) (after backward integration in time). (b) Phase error as a function of time.

Equations (A1)–(A3), (A5), and (A7) are equal to the single layer special case of the transient interface equations by Grue.[20] Equations (A4), (A6), and (A8) are results of further expansions, and it is these versions which are implemented. When the expansions are taken further, the kernels decay faster, and the integration domain can be reduced. This is important for the computational efficiency since the computations of the remainder integrals usually are dominating. The surface integrals [$T(\tilde{\phi})$ and $N(V)$] cannot be expanded further without the convolution terms becoming unstable. The bottom integrals [$T_B(\tilde{\phi})$] and [$N_B(V)$], however, probably can be expanded further, possibly until the remainder integrals become smaller than other errors, and could be ignored. This is related to the factor $e_h \equiv e^{-2kh}$ which appears in the convolution terms taken out from the bottom integrals. This factor is numerically fortunate since it acts like a low-pass filter, allowing even the quartic (and probably higher-order) convolutions to be unhampered by high-frequency noise. Also, optimization could be made by using different integration lengths for each remainder integral. In practical use, very fast primary simulations can be made by omitting all remainder integrals.

APPENDIX B: TEST OF ACCURACY AND CONVERGENCE

Tests of the method's accuracy and convergence are given in Ref. 21, but a couple of additional tests which are relevant for the current work are given here. One way of testing the accuracy of the model is to compare results from a simulation with an analytical solution. Since we here study the instability of Stokes waves, it is natural to test whether an unperturbed Stokes wave is allowed to propagate with the right celerity and without changing its shape. Figure 15(a) shows a Stokes wave at $k_0h=1$ with $ak_0=0.20$ at $t/T=0$ and 1000. The phase shift is only 8.5°, proving the accuracy of the results even after such a long-time integration of a strongly nonlinear problem. We reversed the time after 1000

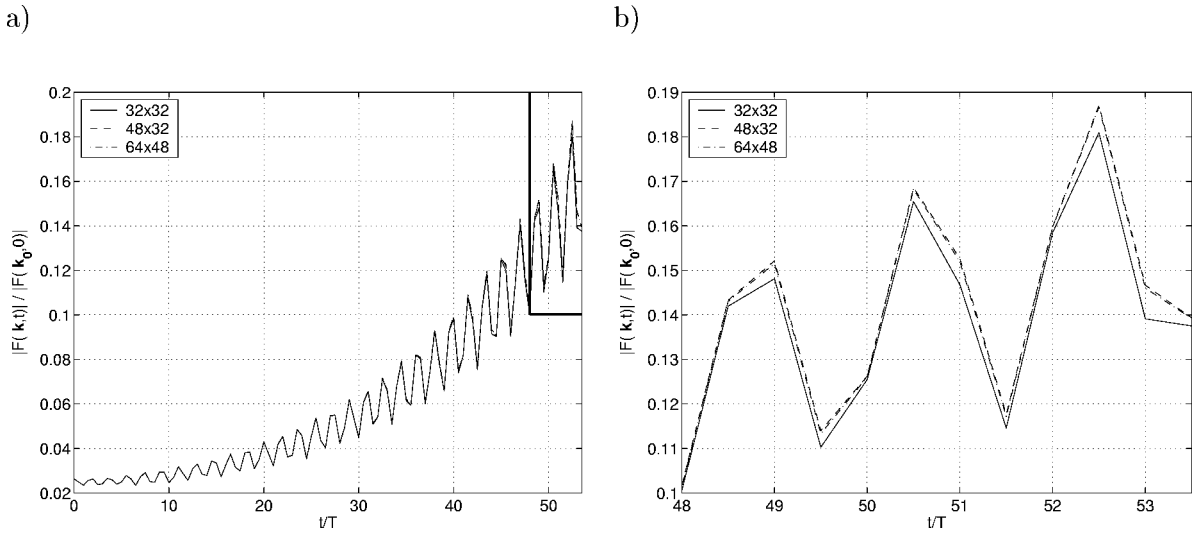

FIG. 16. (a) Convergence test for the oscillating horseshoe pattern in Fig. 9(a) with $k_0h=1$, $ak_0=0.16$. The temporal evolution of the perturbation amplitude is plotted with different resolutions. The legend gives the number of points per longitudinal wavelength times the number of points per horseshoe in the transverse direction. (b) Zoom-in on the results for the last part of the simulation.

periods and simulated back to $t=0$, almost perfectly recovering the initial state. This proves that round-off errors and errors due to the time integrator are extremely small. The phase error as a function of time is shown in Fig. 15(b). The resolution and integration lengths were as usual for simulations in this paper (96×16 points to resolve two Stokes waves and integration domains of $[-\lambda_S/2,\lambda_S/2]\times[-\lambda_c/4,\lambda_c/4]$, where λ_c is set equal to the Stokes wavelength λ_S since there is no perturbation here). We used only one iteration for implicit terms in V, thereby showing that this is sufficient to give a very good accuracy. When the steepness is increased to 0.268 (85% of the maximal steepness), the phase shift is 10° after 100 periods with the same computational parameters, i.e., still showing good accuracy. Only when the steepness passes 90% of the maximal steepness, a higher resolution is necessary to avoid considerable numerical noise. Hence, we see that we can simulate up to a point close to physical breaking before numerical blowup occurs.

A test of convergence is made by doing a simulation of an oscillating horseshoe pattern at $k_0h=1$ with $ak_0=0.16$. Figure 16 shows the temporal evolution of the perturbation amplitude with different resolutions. The resolution which is used in Fig. 9(a) and in simulations of other five-wave interactions in this paper corresponds to 48×32. We see that all three curves are close, and that the two curves with the finest resolution are much closer to each other than to the curve with the coarsest resolution, hence showing excellent convergence.

[1] M.-Y. Su, "Three-dimensional deep-water waves. Part 1. Experimental measurement of skew and symmetric wave patterns," J. Fluid Mech. **124**, 73 (1982).
[2] M.-Y. Su, M. Bergin, P. Marler, and R. Myrick, "Experiments on nonlinear instabilities and evolution of steep gravity-wave trains," J. Fluid Mech. **124**, 45 (1982).
[3] W. K. Melville, "The instability and breaking of deep-water waves," J. Fluid Mech. **115**, 165 (1982).
[4] F. Collard and G. Caulliez, "Oscillating crescent-shaped water wave patterns," Phys. Fluids **11**, 3195 (1999).
[5] J. W. McLean, Y. C. Ma, D. U. Martin, P. G. Saffman, and H. C. Yuen, "Three-dimensional instability of finite-amplitude water waves," Phys. Rev. Lett. **46**, 817 (1981).
[6] J. W. McLean, "Instabilities of finite-amplitude water waves," J. Fluid Mech. **114**, 315 (1982).
[7] J. W. McLean, "Instabilities of finite-amplitude gravity waves on water of finite depth," J. Fluid Mech. **114**, 331 (1982).
[8] M. Stiassnie and L. Shemer, "Energy computations for evolution of class I and II instabilities of Stokes waves," J. Fluid Mech. **174**, 299 (1987).
[9] V. I. Shrira, S. I. Badulin, and C. Kharif, "A model of water wave 'horse-shoe' patterns," J. Fluid Mech. **318**, 375 (1996).
[10] F. Dias and C. Kharif, "Nonlinear gravity and capillary-gravity waves," Annu. Rev. Fluid Mech. **31**, 301 (1999).
[11] W. Craig, "On the Badulin, Kharif and Shrira model of resonant water waves," Physica D **152–153**, 434 (2001).
[12] S. Y. Annenkov and V. I. Shrira, "Sporadic wind wave horse-shoe patterns," Nonlinear Processes Geophys. **6**, 27 (1999).
[13] S. Y. Annenkov and V. I. Shrira, "Physical mechanisms for sporadic wind wave horse-shoe patterns," Eur. J. Mech. B/Fluids **18**, 463 (1999).
[14] M. Xue, H. Xü, Y. Liu, and D. K. P. Yue, "Computations of fully nonlinear three-dimensional wave-wave and wave-body interactions. Part 1. Dynamics of steep three-dimensional waves," J. Fluid Mech. **438**, 11 (2001).
[15] D. R. Fuhrman, P. A. Madsen, and H. B. Bingham, "A numerical study of crescent waves," J. Fluid Mech. **513**, 309 (2004).
[16] D. Fructus, C. Kharif, M. Francius, Ø. Kristiansen, D. Clamond, and J. Grue, "Dynamics of crescent water wave patterns," J. Fluid Mech. (in press).
[17] C. Kharif and M. Francius, personal communications (2003).
[18] M.-Y. Su and A. W. Green, "Coupled two- and three-dimensional instabilities of surface gravity waves," Phys. Fluids **27**, 2595 (1984).
[19] D. Clamond and J. Grue, "A fast method for fully nonlinear water-wave computations," J. Fluid Mech. **447**, 337 (2001).
[20] J. Grue, "On four highly nonlinear phenomena in wave theory and marine hydrodynamics," Appl. Ocean. Res. **24**, 261 (2002).
[21] D. Fructus, D. Clamond, J. Grue, and Ø. Kristiansen, "An efficient model for three-dimensional surface wave simulations, Part I: Free surface problems," J. Comput. Phys. **205**, 665 (2005).
[22] J. D. Fenton, "The numerical solution of steady water wave problems," Comput. Geosci. **14**, 357 (1988).
[23] L. Shemer and M. Stiassnie, in *The Ocean Surface*, edited by Y. Toba and H. Mitsuyasu (D. Reidel, 1985), pp. 51–57.
[24] M.-Y. Su, "Evolution of groups of gravity waves with moderate to high steepness," Phys. Fluids **25**, 2167 (1982).